# Cool gas in brightest cluster galaxies

Oonk, J.B.R.

# Chapter 4

The dust destruction timescales in the cores of clusters of galaxies are relatively short given their high central gas densities. However, substantial mid-infrared and sub-mm emission has been detected in many brightest cluster galaxies. In this letter we present *Herschel* PACS and SPIRE photometry of the brightest cluster galaxy in three strong cooling flow clusters, A1068, A2597 and Zw3146. This photometry indicates that a substantial mass of cold dust is present ($> 3 \times 10^7$ $M_\odot$) at temperatures significantly lower (20–28 K) than previously thought based on limited MIR and/or sub-mm results. The mass and temperature of the dust appear to match those of the cold gas traced by CO with a gas-to-dust ratio of 80–120.

*A&A* 518, L47 (2010)

A. C. Edge[1], J. B. R. Oonk[2], R. Mittal[3], S. W. Allen[4], S. A. Baum[3], H. Böhringer[5], J. N. Bregman[6], M. N. Bremer[7], F. Combes[8], C. S. Crawford[9], M. Donahue[10], E. Egami[11], A. C. Fabian[9], G. J. Ferland[12], S. L. Hamer[1], N. A. Hatch[13], W. Jaffe[2], R. M. Johnstone[9], B. R. McNamara[14], C. P. O'Dea[15], P. Popesso[5], A. C. Quillen[16], P. Salomé[8], C. L. Sarazin[17], G. M. Voit[10], R. J. Wilman[18], M. W. Wise[19]

[1] Institute for Computational Cosmology, Department of Physics, Durham University, Durham, DH1 3LE, UK
[2] Leiden Observatory, Leiden University, P.B. 9513, Leiden 2300 RA, The Netherlands
[3] Chester F. Carlson Center for Imaging Science, Rochester Institute of Technology, Rochester, NY 14623, USA
[4] Kavli Institute for Particle Astrophysics and Cosmology, Stanford University, 452 Lomita Mall, Stanford, CA 94305-4085, USA
[5] Max-Planck-Institut für extraterrestrische Physik, 85748 Garching, Germany
[6] University of Michigan, Dept. of Astronomy, Ann Arbor, MI 48109, USA
[7] H H Wills Physics Laboratory, Tyndall Avenue, Bristol BS8 1TL, UK
[8] Observatoire de Paris, LERMA, CNRS, 61 Av. de l'Observatoire, 75014 Paris, France
[9] Institute of Astronomy, Madingley Rd., Cambridge, CB3 0HA, UK
[10] Michigan State University, Physics and Astronomy Dept., East Lansing, MI 48824-2320, USA
[11] Steward Observatory, University of Arizona, 933 N. Cherry Avenue, Tucson, AZ 85721, USA
[12] Department of Physics, University of Kentucky, Lexington KY 40506 USA
[13] School of Physics and Astronomy, University of Nottingham, University Park, Nottingham NG7 2RD, UK
[14] Department of Physics & Astronomy, University of Waterloo, 200 University Avenue West, Waterloo, Ontario, Canada N2L 3G1
[15] Department of Physics, Rochester Institute of Technology, 84 Lomb Memorial Drive, Rochester, NY 14623-5603, USA
[16] Department of Physics and Astronomy, University of Rochester, Rochester, NY 14627, USA
[17] Department of Astronomy, University of Virginia, P.O. Box 400325, Charlottesville, VA 22904-4325, USA
[18] School of Physics, University of Melbourne, Victoria 3010, Australia
[19] ASTRON, Netherlands Institute for Radio Astronomy,P.O. Box 2, 7990 AA Dwingeloo, The Netherlands

## 4.1 Introduction

The cores of cluster of galaxies are very energetic regions with a high X-ray emissivity, particle density, cosmic ray flux, stellar density and AGN radiation. In this very hostile environment any dust grains are unlikely to survive for more than a few million years due to the action of collisional sputtering (Dwek & Arendt 1992) unless they are shielded (Fabian et al. 1994). It is therefore somewhat surprising to find that dust continuum emission from the brightest cluster galaxies in the most rapidly cooling clusters being detected at sub-mm and MIR wavelengths (Edge et al. 1999, Egami et al. 2006, O'Dea et al. 2008). The presence of cold molecular gas (Edge 2001, Salomé & Combes 2003) and dust absorption in HST imaging (McNamara et al 1996) implies that the dust continuum traces a substantial, cold component to the ISM in these massive elliptical galaxies. However, the origin of the dust and how it is shielded are still poorly understood.

The limitations with the current observations of dust emission make it difficult to establish an unambiguous dust mass as they do not sample over the peak of the dust emission in the FIR. The unprecedented sensitivity of *Herschel* (Pilbratt et al. 2010) to FIR continuum offers the opportunity to accurately constrain the full FIR spectrum of the dust emission in cluster cores. The authors were awarded 140 hours of time in an Open Time Key Project (PI Edge) to investigate the FIR line and continuum properties of a sample of 11 brightest cluster galaxies (BCGs) in well-studied cooling flow clusters selected on the basis of optical emission line and X-ray properties. The full goals of the project are to observe at least five atomic cooling lines for each object that cover a range in density and temperature behaviour and obtain a fully sampled FIR spectral energy distribution. In this paper we present the Photodetector Array Camera & Spectrometer (PACS, Poglitsch et al. 2010) and Spectral and Photometric Imaging REceiver (SPIRE, Griffin et al. 2010) photometry for the three targets observed in the Science Demonstration Phase (SDP), Abell 1068 ($z$ = 0.1386), Abell 2597 ($z$ = 0.0821) and Zw3146 ($z$ = 0.2906). In a parallel paper (Edge et al. 2010), we present the FIR spectroscopy for the first two of these clusters.

The three clusters observed have quite contrasting multiwavelength properties. Abell 1068 and Zw3146 both have strong MIR emission (O'Dea et al. 2008, Egami et al. 2006) with a relatively bright CO detection (Edge 2001) and a weak central radio source (McNamara et al. 2004). A1068 lies just below the luminosity threshold of a ULIRG ($10^{12}$ $L_{\odot}$) and exhibits some contribution from an AGN (Crawford et al. 1999, O'Dea et al. 2008). On the other hand, Abell 2597 is a relatively weak MIR source (Donahue et al. 2007) with a weak CO detection (Salome, priv. comm.) and a powerful central radio source (Sarazin et al. 1995). The implied FIR luminosity of A2597 is a factor of around 30 below that of A1068 and, in addition, the fractional contribution from an AGN in the MIR is also lower in A2597.

## 4.2 Observations

We performed photometric imaging of A1068, A2597 and Zw3146 with PACS and SPIRE. The data were reduced with the *Herschel* Interactive Processing Environment (HIPE) software version 2.3.1436 (Ott 2010). We used for both PACS and SPIRE the official scripts as presented by the PACS and SPIRE ICC teams during the *Herschel* SDP data processing workshop in

December 2009.

### 4.2.1 PACS Data

The PACS photometric observations were taken in LargeScanMapping mode in all three bands of the photometer, BS (70 $\mu$m), BL (100 $\mu$m) and R (160 $\mu$m) using the medium scan speed ($20''s^{-1}$). The scan maps comprised 18 scan line legs of $4'$ length and cross-scan step of $15''$. Each observation had a "scan" and an orthogonal "cross-scan" direction and we calibrated the corresponding data separately before combining them into a single map of $9^{'} \times 9^{'}$. The resulting maps have a resolution of $5.2''$, $7.7''$ and $12''$ at 70, 100 and 160 $\mu$m, respectively and are presented in the electronic version of this paper. The PACS photometer performs dual-band imaging such that the BS and BL bands each have simultaneous observations in the R band so we have two sets of scans in the R band.

We adopted the PACS Data Reduction Guideline to process the raw level-0 data to calibrated level 2 products and used the official script for PACS ScanMapping mode but with particular attention to the high pass filtering to remove "$1/\sqrt{f}$" noise. We choose to use the *HighPassFilter* method with a filter of 20 readouts which will remove structure on all scales above $82''$. The target BCG and other bright sources in the field were masked prior to applying the filter. The size of the mask was chosen to be less than the filter size so as to minimize any left-over low-frequency artefacts under the masks. We used masks with a radius of $15''$ for our sources. We tried varying the size for the filter from 10 to 30 readouts and the mask radius from 10–$30''$ and found our results to not change significantly for these ranges in values. Finally the task 'photProject', was used to project the calibrated data onto a map on the sky in units of Jy pixel$^{-1}$. The "scan" and "cross-scan" maps were then averaged to produce the final coadded map. The PACS and SPIRE images are included in the electronic version of the paper. The spatial flux distribution and flux densities of our target sources were investigated using cumulative flux curves. The spatial flux distribution for each of our three sources is consistent with that expected from a point source. Flux densities in the BS, BL and R band were extracted using a $33''$ by $33''$ aperture centered on the BCG. Small aperture corrections were applied as outlined in the PACS Scan Map release note (PICC-ME-TN-035). Care was taken to calibrate these derived flux densities to account for the known flux overestimation in the used HIPE version by factors 1.05, 1.09 and 1.29 in BS, BL and R bands respectively. The absolute flux accuracy is within 10 % for BS and BL, and better than 20 % for R. These uncertainties are not believed to be correlated due to the BS and BL bands being taken at different times and the R band using a different detector.

### 4.2.2 SPIRE Data

The SPIRE photometry was performed in the LargeScanMap mode with cross-linked scans in two orthogonal scan directions. The photometer has a field of view of $4^{'} \times 8^{'}$, which is observed simultaneously in three spectral bands, PSW (250 $\mu$m), PMW (350 $\mu$m) and PLW (500 $\mu$m) with a resolution of about $18''$, $25''$ and $36''$, respectively. The resulting maps measure $12^{'} \times 12^{'}$ in size and are presented in the electronic version of this paper.

We used the standard HIPE pipeline for the LargeScanMap observing mode and the naïve map-maker. The pre-processed raw telemetry data were first subject to engineering conversion

wherein the raw timeline data were converted to meaningful units, the SPIRE pointing product was created, deglitching and temperature drift correction were performed, and maps were created, the units of which were Jy beam$^{-1}$. Our targets are unresolved at the spatial resolution of SPIRE. We derived their flux densities by fitting the sources with the SPIRE point source response function. Care was taken to de-blend our target from other nearby sources at the longer wavelengths, where the sources are most likely to be background to the cluster. We account for the known flux calibration offset in the used version of HIPE by applying the following multiplicative calibration factors 1.02, 1.05 and 0.94 to the derived flux densities in the PSW, PMW and PLW bands respectively (see Griffin et al. 2010, Swinyard et al. 2010). We also performed aperture photometry using the HIPE point-source extraction (PSE) tool but this method gives accurate results only for isolated point sources. At 350 $\mu$m and 500 $\mu$m, the BCGs in A2597 and Zw3146 are close to the detection limit and at the confusion limit of SPIRE making the PSE method of determining the fluxes unsuccessful. A1068 has a relatively strong compact BCG in far infrared and so we performed the PSE to find that the flux estimates using AIPS and HIPE agree with each other to better than 5%.

## 4.3 Results

In the PACS photometry, A1068, A2597 and Zw3146 have been detected in all three bands. For A1068, 70 and 100$\mu$m values are slightly less than the *IRAS* 60 and 100 $\mu$m measurements. This could be due to nearby sources that cannot be separated from the BCG in the much lower resolution *IRAS* observations but no sufficiently bright source is visible in our PACS imaging. There is a large difference between the *Spitzer* MIPS 70$\mu$m flux (Quillen et al. 2008) and our PACS 70$\mu$m flux, the PACS flux being a factor 1.7 lower than the MIPS flux. In the case of Zw3146 the MIPS and PACS 70 $\mu$m fluxes also differ with the PACS value being a factor 1.4 larger than the MIPS value (Egami et al. 2006). For A2597 the PACS fluxes differ from the *Spitzer* 70 and 160 $\mu$m fluxes reported by Donahue et al. (2007). Part of this difference was resolved when the MIPS 70 $\mu$m data were re-analysed and found to be a factor of two too high (Donahue, priv. comm.). The differences observed between the PACS and *Spitzer* fluxes require further investigation. In the SPIRE photometry, A1068 is detected in all three SPIRE bands. A2597 and Zw3146, while clearly detected in PSW and PMW bands, have a 1–2 $\sigma$ detection in the PLW band. Table 1 gives the photometric results for the three galaxies, with 2$\sigma$ upper-limit for A2597 and Zw3146 in PLW. Figure 1 presents the radio to optical spectral energy distributions (SEDs) for the three targets. These plots show the significant variation in the relative radio-FIR-optical contributions for each of our galaxies. Here we focus on the sub-mm/MIR dust emission as sampled by PACS and SPIRE photometry, complemented by published *Spitzer* and *IRAS* measurements.

We fit the SEDs of the dust emission using black bodies modified with a dust emissivity index, $\beta$. The FIR-MIR slopes of our sources require the presence of at least two dust components. Previous studies of star-forming galaxies have indeed established that a single modified black body (MBB) is inadequate to account for the observed dust emission (Wiklind 2003). Hence, our model for the SEDs consists of two MBBs with the dust emissivity index for each fixed to $\beta$=2 and a mass absorption coefficient, $\kappa_{\rm d\nu}$, of 2.5 m$^2$ kg$^{-1}$ at 100$\mu$m.

For A1068 we fit the 24–850$\mu$m emission. For A2597 and Zw3146 the SCUBA 850$\mu$m

**Table 4.1 —** Log of *Herschel* Observations. The *Spitzer* data are from Quillen et al. (2008), Donahue et al. (2007, priv. comm.) and Egami et al. (2006). The SCUBA data are from Edge (priv. comm.), Zemcov et al. (2007) and Chapman et al. (2002).

| Cluster | $z$ | Instrument | $\lambda$ ($\mu$m) | Obsid | Flux (mJy) |
|---|---|---|---|---|---|
| A1068 | 0.1386 | PACS | 70 | 1342187051 | 542±6 |
| | | PACS | 100 | 1342187053 | 757±6 |
| | | PACS | 160 | | 769±4 |
| | | SPIRE | 250 | 1342187321 | 376±6 |
| | | SPIRE | 350 | | 135±6 |
| | | SPIRE | 500 | | 56±8 |
| | | SCUBA | 450 | | 39±13 |
| | | SCUBA | 850 | | 5.3±1.1 |
| | | *Spitzer* | 24 | | 74.5±2.0 |
| | | *Spitzer* | 70 | | 941±30 |
| | | *IRAS* | 60 | | 577±52 |
| | | *IRAS* | 100 | | 958±144 |
| A2597 | 0.0821 | PACS | 70 | 1342187118 | 57±5 |
| | | PACS | 100 | 1342187120 | 67±7 |
| | | PACS | 160 | | 86±4 |
| | | SPIRE | 250 | 1342187329 | 30±6 |
| | | SPIRE | 350 | | 15±6 |
| | | SPIRE | 500 | | < 16 |
| | | SCUBA | 850 | | 14.5±2.3 |
| | | *Spitzer* | 24 | | 2.1±0.2 |
| | | *Spitzer* | 70 | | 49±6 |
| | | *Spitzer* | 160 | | 52±3 |
| Zw3146 | 0.2906 | PACS | 70 | 1342187043 | 94±6 |
| | | PACS | 100 | 1342187045 | 150±6 |
| | | PACS | 160 | | 139±5 |
| | | SPIRE | 250 | 1342187326 | 81±6 |
| | | SPIRE | 350 | | 30±6 |
| | | SPIRE | 500 | | < 16 |
| | | SCUBA | 450 | | <48 |
| | | SCUBA | 850 | | 6.6±2.6 |
| | | *Spitzer* | 24 | | 4.1±0.4 |
| | | *Spitzer* | 70 | | 68±14 |
| | | *Spitzer* | 160 | | 157±35 |

detections have been removed and we fit only the 24–350$\mu$m range. In the case of A2597, this is due to the unknown amount of radio contamination at 850$\mu$m. In the case of Zw3146 the BCG is blended with strong background source at 850$\mu$m (Chapman et al. 2002). The data are weighted in the fit inversely to the square of their error. The resulting fits are shown in Figure 1. The derived dust temperatures and total FIR luminosities for each source are listed in Table 2.

The results in Table 2 indicate that at least two dust components, one at 20–25 K and one at 50–60 K, are present in all three sources. The FIR emission is much stronger relative to the optical in A1068 and Zw3146 as compared to A2597. The SEDs of A1068 and Zw3146 resemble those of strongly star-forming systems and, based on the total FIR luminosity derived here, we find star formation rates (SFR) of 60 and 44 $M_\odot$ yr$^{-1}$ in these two systems using the Kennicutt (1998) conversion factor. For A2597 a much more modest SFR of 2 $M_\odot$ yr$^{-1}$ is inferred. These values are comparable to SFRs derived from H$\alpha$ line and/or UV continuum emission given the uncertainties of these tracers. However, the SFR values derived from *Spitzer* data are higher for A1068 and Zw3146. The difference for A1068 is the most pronounced and can be directly attributed to the stronger AGN contribution in this object (Quillen et al. 2008) which boosts the 24$\mu$ flux compared other comparable sources. Therefore, when the total FIR luminosity is derived from the 15$\mu$m flux infered from *Spitzer* it will be overestimated. The value for Zw3146 from Egami et al. (2006) is higher than ours as their fit includes the SCUBA 850$\mu$m point from Chapman et al. (2002) which appears to be overestimated on the basis of our SPIRE data.

The gas to dust ratio is found to be between 80 and 140 (see Table 2). Gas temperatures can be inferred from CO measurements (Edge 2001, Salome & Combes 2003). These estimates infer gas temperatures of 25–40 K thus implying that the gas and dust share a common environment and are potentially co-located in the denser regions of cold, molecular gas clouds. We have attempted to determine how much extended emission is present from our highest spatial resolution PACS 70$\mu$m image but we find no evidence for more than 10% additional flux beyond a point source. Clearly these limits will improve with a better characterisation of the instrument but we believe that we can conclude that the dust emission in our targets has an extent comparable to that the bulk of the CO emitting gas and optical emission lines ($< 5''$ or 5–20 kpc).

## 4.4 Discussion and conclusions

Our initial *Herschel* results confirm the presence of the striking dust emission peak expected from the observations at sub-mm (Edge et al. 1999, Chapman et al. 2002) and MIR (Egami et al. 2006, O'Dea et al. 2008).

The star formation rates derived from the full-sampled FIR SED are comparable to those derived from *Spitzer* 24$\mu$m fluxes apart from A1068, which has the strongest contribution from an AGN so hot dust dominates to the 24$\mu$m flux. However, in the sub-mm the contribution from the radio continuum from an active nucleus must be correctly accounted for before any dust mass can be estimated from the 850$\mu$m flux. In the case of A2597 here and A2390 in Edge et al. (1999), the presence of a powerful radio source appears to contribute to the SCUBA 850$\mu$m flux.

**Table 4.2 —** Summary of results and other cluster properties. The *Spitzer* SFR values are from O'Dea et al. (2008), Donahue et al. (2007) and Egami et al. (2006). The Optical/UV SFR values are from McNamara et al. (2004), Donahue et al. (2007) and Egami et al. (2006). The CO gas masses are from Edge (2001) and Salomé (priv. comm.) and the H$\alpha$ slit luminosities are from Crawford et al. (1999).

| Cluster | A1068 | A2597 | Zw3146 |
|---|---|---|---|
| Dust Temperatures | 24±4K | 21±6K | 23±5K |
| | $57^{+12}_{-4}$K | $48^{+17}_{-5}$K | $53^{+22}_{-6}$K |
| Cold Dust Mass | $5.1\times10^{8}$ $M_\odot$ | $2.3\times10^{7}$ $M_\odot$ | $5.4\times10^{8}$ $M_\odot$ |
| Warm Dust Mass | $3.9\times10^{6}$ $M_\odot$ | $2.9\times10^{5}$ $M_\odot$ | $1.9\times10^{6}$ $M_\odot$ |
| Total FIR Luminosity | $3.5\times10^{11}$ $L_\odot$ | $8.8\times10^{9}$ $L_\odot$ | $2.5\times10^{11}$ $L_\odot$ |
| Star Formation Rate | 60±20 $M_\odot$ $yr^{-1}$ | 2±1 $M_\odot$ $yr^{-1}$ | 44±14 $M_\odot$ $yr^{-1}$ |
| SFR *Spitzer* | 188 $M_\odot$ $yr^{-1}$ | 4 $M_\odot$ $yr^{-1}$ | 70±14 $M_\odot$ $yr^{-1}$ |
| SFR *optical/UV* | 20–70 $M_\odot$ $yr^{-1}$ | 10–15 $M_\odot$ $yr^{-1}$ | 47±5 $M_\odot$ $yr^{-1}$ |
| CO gas mass | $4.1\times10^{10}$ $M_\odot$ | $2.0\times10^{9}$ $M_\odot$ | $7.7\times10^{10}$ $M_\odot$ |
| H$\alpha$ Slit Luminosity | $8\times10^{41}$ erg $s^{-1}$ | $3\times10^{41}$ erg $s^{-1}$ | $3\times10^{42}$ erg $s^{-1}$ |

While it is difficult to draw any general conclusions from just three BCGs, we note with interest that the ratio of dust mass to CO-derived gas mass is constistent for all three within a factor of five. If the dust were mostly generated through dust ejection from evolved stars then the dust mass should closely correlate with the total stellar mass. However, our three galaxies have very similar optical/NIR absolute magnitudes. So, unless the ejected dust were "captured" by the cold gas clouds protecting it from X-ray sputtering, this suggests that the apparent correlation between the molecular gas and dust masses arises from a direct connection between the gas reservoir and star formation.

These results are a limited example of those to come in the very near future from *Herschel* as there are two other Open Time Key Projects (PI Egami and Smith) that are targetting a total of 70 clusters that cover a broad range of BCG properties so the wider context of these initial observations can be determined. In particular, the amount of dust present in more quiescent BCGs and other massive cluster ellipticals will be important in assessing how much of the dust seen in cool core BCGs orginates from the underlying stellar population.

## 4.5 Acknowledgements

We would like to thank the *Herschel* Observatory and instrument teams for the extraordinary dedication they have shown to deliver such a powerful telescope. We would like to thank the HSC and NHSC consortium for help with data reduction pipelines. J.B.R.O. thanks HSC, the *Herschel* Helpdesk and the PACS group at MPE for useful discussions. R. M. thanks the NHSC for the HIPE tutorials.

## Bibliography

Chapman, S. C., Scott, D., Borys, C., et al. 2002, MNRAS, 330, 92
Crawford, C. S., Allen, S. W., Ebeling, H., et al. 1999, MNRAS, 306, 857

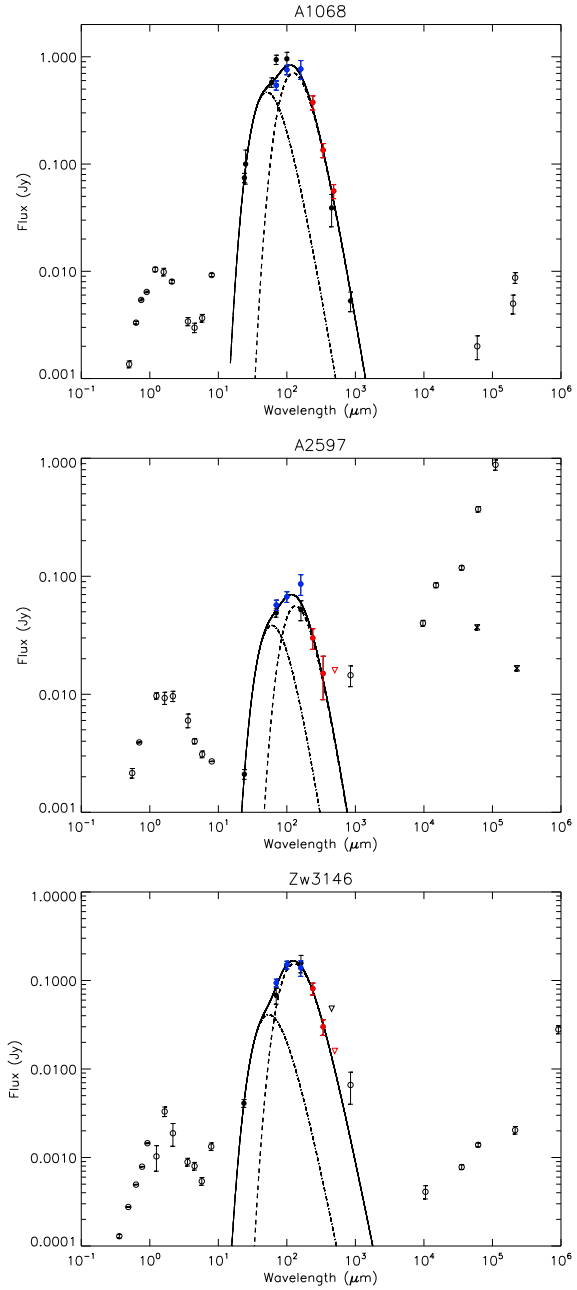


**Figure 4.1 —** Spectral energy distributions for A1068 (top), A2597 (middle) and Zw3146 (bottom) including *Herschel* PACS/SPIRE, *Spitzer*, Radio, NIR photometry from 2MASS and optical photometry from SDSS. To account for absolute flux uncertainties we have set the following errors on the fluxes derived from the various instruments (unless the quoted error is larger than this); PACS BS/BL 10%, PACS R 20%, SPIRE 15%, *Spitzer* 10%, SCUBA 450 $\mu$m 30% and SCUBA 850 $\mu$m 20%. The model fit to the sub-mm/FIR/MIR data is shown by the black solid line. Only filled symbols have been used in the fit. The two modified blackbodies making up the model are shown by the black long dash and dash-dot lines. For A2597 we also show two VLBI measurements (black crosses) of the BCG core at 1.3 and 5 GHz (Taylor et al. 1999). These points show that the BCG has a strong, inverted radio core.

Donahue, M., Jordán, A., Baum, S. A., et al. 2007, ApJ, 670, 231
Dwek, E., & Arendt, R. G., 1992, ARA&A, 30, 11
Edge, A. C., Ivison, R. J., Smail, I. R., et al., 1999, MNRAS, 306, 599
Edge, A. C., 2001, MNRAS, 328, 762
Edge, A. C., Oonk, J. B. R., Mittal, R., et al. 2010, A&A, this volume
Egami, E., Misslet, K. A., Rieke, G. H., et al. 2006, ApJ, 647, 922
Fabian, A. C., Johnstone, R. M., & Daines, S. J., 1994, MNRAS, 271, 737
Griffin, M., Abergel, A., Abreu, A., et al. 2010, this volume
Kennicutt, R. C. 1998, ARA&A, 36, 189
McNamara, B. R., Wise, M. W., Sarazin, C. L., et al. 1996, ApJ 466, L9
McNamara, B. R., Wise, M. W., & Murray, S. S., 2004, ApJ, 601, 173
O'Dea, C. P., Baum, S. A., Privon, G., et al. 2008, ApJ, 681, 1035
Ott, S. 2010 in ASP Conference Series, Astronomical Data Analysis Software and Systems XIX, Y. Mizumoto, K. I. Morita, and M. Ohishi, eds., in press
Pilbratt, G., et al. 2010, A&A, this volume
Poglitsch, A., et al. 2010, A&A, this volume
Quillen, A. C., Zufelt, N., Park, J., et al. 2008, ApJS, 176, 39
Salomé, P., & Combes, F. 2003, A&A, 412, 657
Sarazin, C. L., Burns, J. O., Roettiger, K., et al. 1995, ApJ, 447, 559
Swinyard, B., Griffin, M., Ade, P., et al. 2010, A&A, this volume
Taylor, G. B., O'Dea, C. P., Peck, A. B., et al. 1999, ApJ 512, L27
Wiklind, T. 2003, ApJ, 588, 736
Zemcov, M., Borys, C., Halpern, M., et al. 2007, MNRAS, 376, 1073

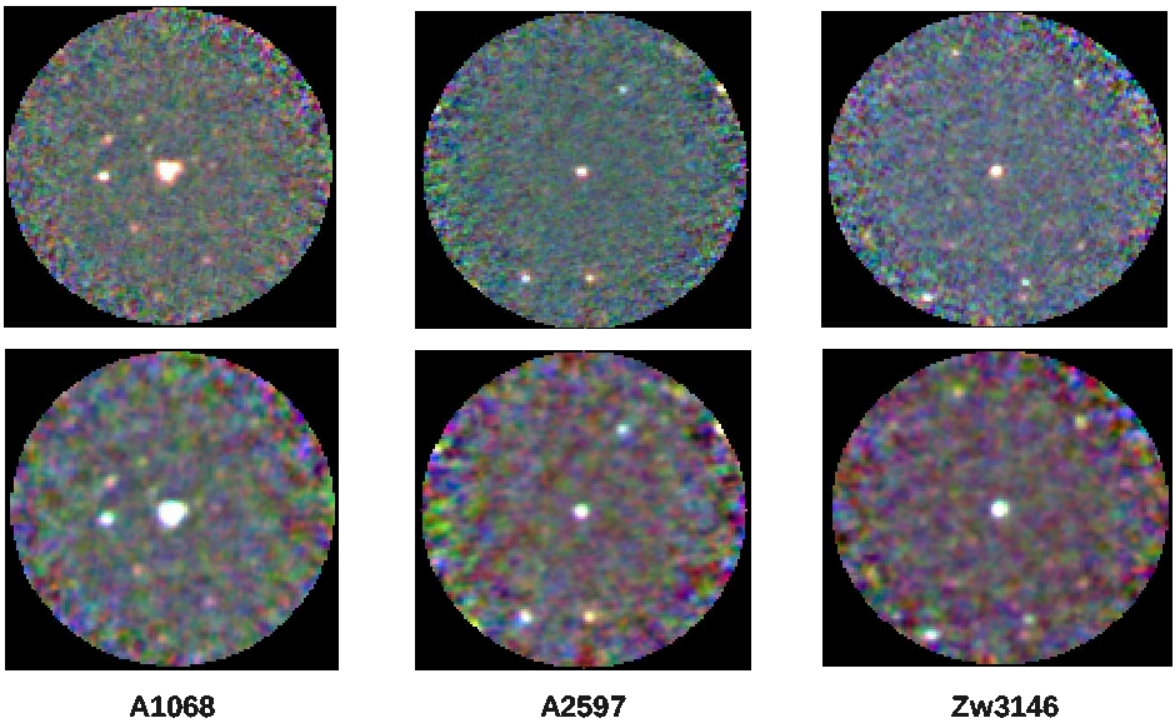


**Figure 4.2 —** Combined images from the three PACS bands (BS, BL and R in the blue, green and red channels) for the three clusters within radius of 2.5′ of the BCG The top row are images combined in their original resolution and the bottom row are the images combined with a common smoothing of 12″ to match resolution. The images are only available in colour in the online version.

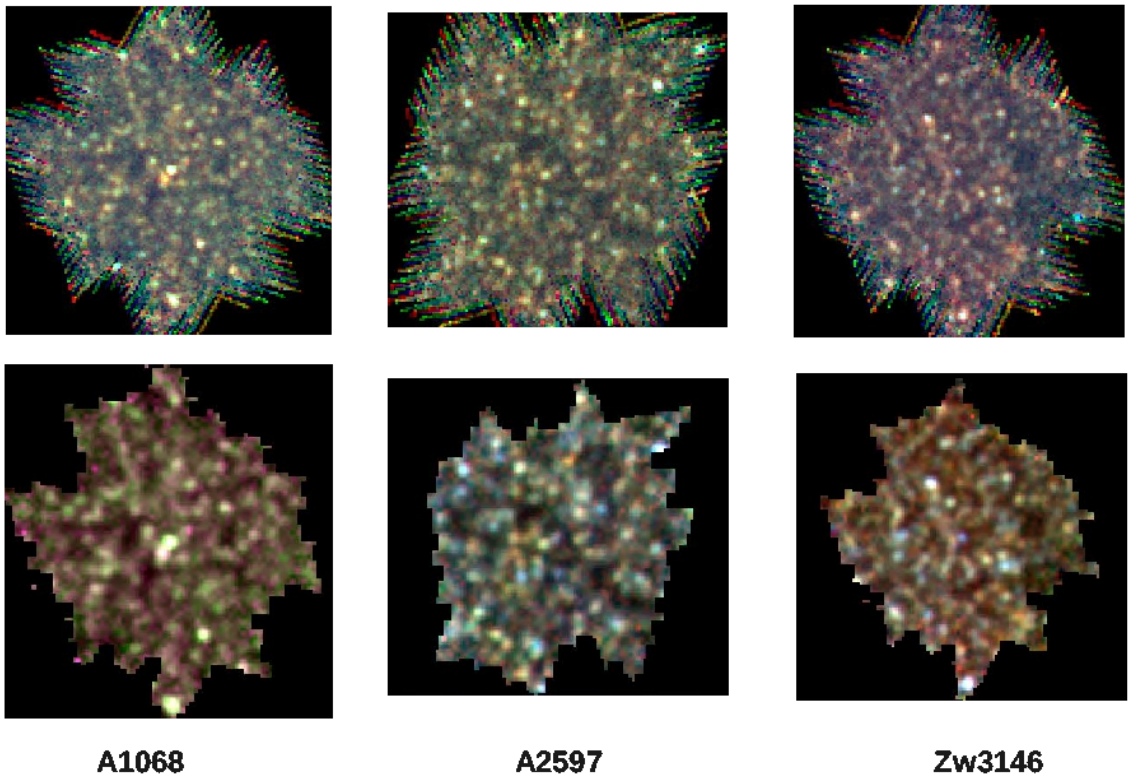


**Figure 4.3 —** Combined images from the three SPIRE bands (PSW, PMW and PLW in the blue, green and red channels) for full field covered for the three clusters covering approximately $12' \times 12'$. The top row are images combined in their original resolution and the bottom row are the images combined with a common smoothing of $36''$ to match resolution and clipped to remove areas of low exposure. The BCG is at the centre of the image and in A2597 and Zw3146 is the bluest object present (see text). The images are only available in colour in the online version.